

# Power law behavior related to mutual synchronization of chemically coupled map neurons

I. Franović and V. Miljković<sup>a</sup>

Faculty of Physics, University of Belgrade, P.O. Box 368, 11001 Belgrade, Serbia

Received 26 December 2009 / Received in final form 20 April 2010

Published online 29 June 2010 – © EDP Sciences, Società Italiana di Fisica, Springer-Verlag 2010

**Abstract.** The widely represented network motif, constituting an inhibitory pair of bursting neurons, is modeled by chaotic Rulkov maps, coupled chemically via symmetrical synapses. By means of phase plane analysis, that involves analytically obtaining the curves guiding the motion of the phase point, we show how the neuron dynamics can be explained in terms of switches between the noninteracting and interacting map. The developed approach provides an insight into the observed time series, highlighting the mechanisms behind the regimes of collective dynamics, including those concerning the emergent phenomena of partial and common oscillation death, hyperpolarization of membrane potential and the prolonged quiescence. The interdependence between the chaotic neuron series takes the form of intermittent synchronization, where the entrainment of membrane potential variables occurs within the sequences of finite duration. The contribution from the overlap of certain block sequences embedding emergent phenomena gives rise to the sudden increase of the parameter characterizing synchronization. We find its onset to follow a power law, that holds with respect to the coupling strength and the stimulation current. It is established how different types of synaptic threshold behavior, controlled by the gain parameter, influence the values of the scaling exponents.

## 1 Introduction

Recently, important advances have been made in understanding the role of network motifs, identified as the elementary building blocks on both the structural and functional levels of organization in a variety of networks [1,2]. For neural networks [3–5], there is evidence that the wiring within and between the motifs allows them to preserve substantial degree of operational autonomy [6,7]. The genesis of simple biological rhythms by central pattern generators (CPGs) [8,9], as well as the primary activity modes of neurons in specific brain areas [10–13], validate the study of motifs of bursting neurons, whose dynamics typically assumes chaotic form [14]. Focusing on the cooperative behavior among chaotic units, the analysis of synchronization phenomena stands out as an ever growing field of interest. The current research disclosed several types of chaotic synchronization, including complete or full synchronization [15], generalized synchronization [16], phase synchronization [17], intermittent synchronization [18–20] and lag synchronization [21]. So far, three of these types have been known to occur in case of networks of bursting neurons [22,23]: individual spike synchronization, complete synchronization and burst synchronization (matching between the timings of the bursts), with the latter sharing the features of chaotic phase synchronization [24].

When dealing with a more involved neuron dynamics that may possess several characteristic time scales, instead of the conductance-based models with systems of ordinary differential equations and multidimensional phase spaces, it is analytically more efficient, and sometimes heuristically plausible to introduce discrete models of neuronal maps. Taking advantage of the bursting decomposition to fast- and slow-scale oscillations [25], Rulkov defined three versions of a two dimensional system of difference equations [26–28], appropriate for capturing different types of the autonomous neuron behavior, as well as the activity modes of coupled neuron systems [10,27–29]. For the isolated neuron, the map we consider yields square-wave bursting, along with silence and chaotic spiking, depending on the selected set of parameters.

Distinguishing from the previous papers, the model of chemical synapse includes the time delay. Even so, we were able to carry over the phase plane analysis from the case of non-interacting to interacting neuron, providing an insight into its dynamics and the possible emergent phenomena. In fact, it is demonstrated how the synaptic properties affect the formation of the interacting map, and more importantly, it is shown how the particular sequences observed in the time series may be explained by the switches between the non-interacting and interacting map. Consequently, the switches can be linked to the emergent phenomena we encounter: partial and common oscillation death (OD) [30–32], hyperpolarization of

<sup>a</sup> e-mail: vladimir.miljkovic@ff.bg.ac.rs

membrane potential and the prolonged quiescence. Varying the synaptic parameters and the neuron stimulation current affects the distribution of these phenomena and the type of sequences in which they occur, reducing the possibility of establishing asymptotically stable regime in the neuron time series [14,33]. Under such circumstances, considering synchronization among the two neurons' series requires an extension beyond chaotic burst synchronization, so as to admit intermittent overlaps between the specific sequences within the time series. In contrast to the genuine asymptotic synchronization, this may be interpreted as an example of intermittent synchronization, thought of as the entrainment of the dynamical variables within random time intervals of finite duration [18].

In order to characterize the degree of synchronization between the two chaotic series, we introduce an appropriate parameter  $R$ , that can be contributed by all the overlapping sequences, regardless of the neurons' activity mode. We find that there exists an area of intrinsic and synaptic parameters, where a sudden rise of  $R$  takes place. Its onset may be described by a power law with respect to both the coupling strength and the magnitude of the external stimulation. It is noteworthy that the emergent phenomena (OD, hyperpolarization) reported here have also been observed in systems of coupled neurons with the more realistic models (Hodgkin-Huxley, Hindmarsh-Rose and Fitzhugh-Nagumo) applied [34–36], and the OD phenomenon has even been anticipated for the pancreatic  $\beta$ -cells [37]. Thus far, it has been considered how the transition to OD can take place from different outgoing regimes, as well as for different sizes of neuron assemblies. An interesting and previously uncovered topic is that of the implications the emergent phenomena may have on synchronization behavior, analyzed here in the case of neuron maps coupled via delayed chemical synapses.

The paper is organized as follows. In Section 2, the phase plane approach is presented as an effective means to explain the time series of both the isolated neuron and the coupled pair, together with introducing the quantity  $R$ , appropriate to characterize synchronization in terms of the observed collective regimes. Section 3 is divided into four subsections, the first three of which concern the  $R$  dependence on synaptic weight  $g_c$  and the details on how it is influenced by the synaptic time delay  $\tau$  and the gain parameter  $k$ , while the fourth subsection deals with the effects of the external bias current  $\sigma$  on  $R$  when the remaining parameters are fixed. Section 4 contains the summary of the results we obtained.

## 2 Model and the method for analyzing mutual synchronization of a neuron pair

In this section we present the factors influencing the bursting dynamics and the irregularity of the isolated neuron's time series (Sect. 2.1), as well as the details of the applied model of chemical synapse and the possible states of the coupled system (Sect. 2.2). In view of the data obtained, we introduce a parameter to characterize the degree of

mutual synchronization and discuss how it is contributed by the different states of the system (Sect. 2.3).

### 2.1 Dynamics of an isolated neuron

We consider a neuron model based on a two-dimensional map, proposed by Rulkov [26], whose dynamics is given by [10,12,13,38,39]

$$\begin{aligned}x_{n+1} &= \frac{\alpha}{1+x_n^2} + y_n, \\y_{n+1} &= y_n - \mu(x_n - \sigma),\end{aligned}\quad (1)$$

where the subscript  $n$  indicates the iteration step. The parameters  $\alpha$  and  $\sigma$  are both  $\mathcal{O}(1)$ , the latter of which simulates the action of the external dc bias current, and  $\mu$  is set to the value  $\mu = 0.001$ . Due to smallness of  $\mu$ ,  $y_n$  variable evolves on a much slower characteristic time scale than  $x_n$ , which justifies the use of terms fast and slow variables for  $x_n$  and  $y_n$ , respectively. In the context of neurobiology,  $x_n$  is assumed to correspond to the membrane potential, whereas for  $y_n$  an analogy to gating variables may be drawn [11,12]. This particular version of the Rulkov map is referred to as chaotic [12], because it is known to generate, apart from silence, the regimes of chaotic spiking and chaotic bursting.

Here we focus on the bursting mechanism, applying the arguments of the fast-slow analysis [10,12,26,27], that treats the slow variable as a control parameter within the fast subsystem, the role stressed in the following by assigning it with  $\gamma$  instead of  $y_n$ . Since  $\gamma$  enters the fast subsystem only additively, it affects the  $x_n$  first return map (Fig. 1a) merely by getting it shifted up (down) when increasing (decreasing). Depending on the value of  $\gamma$ , the map has one fixed point at least, and three at most, with the left and the middle fixed points coalescing and eventually disappearing through a saddle-node bifurcation at  $\gamma = \gamma_{sn}$ . As with other unimodal maps, one can imagine the irregularity in membrane potential series to be associated with the iterates running through a narrow channel arising between the map and the identity line in case  $\gamma > \gamma_{sn}$  [38].

Though the first return map provides a reasonable explanation for chaoticity, a more elaborate phase plane analysis is required for understanding the mechanism of triggering and terminating the bursts. It can be shown that in the  $x$ - $\gamma$  plane the nullclines of the fast subsystem trace out an S-shape curve [10], whose top, middle and bottom branches correspond to the right, middle and left fixed points in Figure 1a, respectively. In terms of dynamical stability, it turns out that the points on the bottom (middle) branch are always stable (unstable), whereas the stability on the top branch changes with  $\gamma$ . With the selected set of parameters, the small  $\gamma$  area of phase plane near the S-curve's left knee, where the points on the top branch become stable, remains inaccessible and therefore irrelevant to the neuron dynamics. Thus, for the analysis on how the isolated neuron bursts, it suffices to present the blowup of the region around the S-curve's right knee

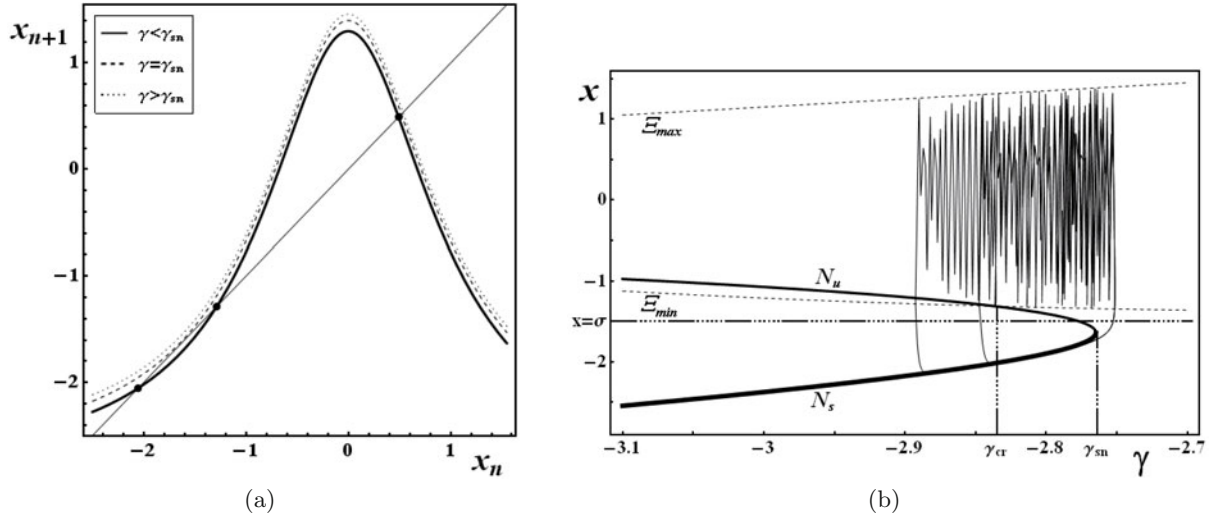


**Fig. 1.** (a) First return map of the fast variable according to the chaotic Rulkov model. The slow evolution of  $y_n$  allows one to consider it as a parameter  $\gamma$  within the fast subsystem. The map is pulled up (down) as  $\gamma$  increases (decreases), which affects the number and the position of the fixed points. For  $\gamma < \gamma_{sn}$  (solid line) the map has three fixed points, at  $\gamma = \gamma_{sn}$  (dashed line) two, while above  $\gamma_{sn}$  (dotted line) a single fixed point remains. Only the left and the middle fixed points are relevant to bursting of an isolated neuron. (b) Bistability region of the fast subsystem, characterized by the coexistence of a stable fixed point and a chaotic attractor. Bursting is influenced by the sections of the two fast nullclines, forming a parabola with branches of stable  $N_s$  and unstable fixed points  $N_u$ . The bursting region is limited by the hard boundary at  $\gamma = \gamma_{sn}$  and the soft boundary at  $\gamma = \gamma_{cr}$ . Bursting requires that the slow variable nullcline  $x_n = \sigma$  lies above the parabola vertex. Amplitudes of the superimposed orbit are determined by the curves of the minimal  $\Xi_{min}$  and maximal  $\Xi_{max}$  iterates of the fast subsystem.

(see Fig. 1b). There the branches of stable  $N_s$  and unstable fixed points  $N_u$  merge into a parabola, with the vertex located at  $\gamma = \gamma_{sn}$ .

The key to bursting lies in the existence of bistability [10,12] in the fast subsystem: within a limited range of  $\gamma$ , along with the stable fixed point, that accounts for silence between the bursts, there is a chaotic attractor, responsible for the rapid spikes constituting a burst. The burst envelopes are provided by the curves of maximal and minimal iterates,  $\Xi_{max}$  and  $\Xi_{min}$ , respectively, that are obtained as the first and second images of zero,  $R(0)$  and  $R^2(0)$  in function of  $\gamma$  [10]. The lower boundary on the  $\gamma$  interval where bistability occurs presents the point  $\gamma = \gamma_{cr}$ , at which the minimum iterate maps onto  $N_u$ , whereas the upper boundary is given by  $\gamma = \gamma_{sn}$ . The arrival of the phase point at the upper (lower) boundary corresponds to triggering (terminating) the burst, with the boundary at  $\gamma_{cr}$  being somewhat “softer” than the one at  $\gamma_{sn}$ . In effect, the chaotic attractor undergoes an external crisis at  $\gamma_{cr}$  [10], that should induce the transition to the quasi-steady state, determined by the stable fixed point. Due to chaotic nature of the map, such transition may be delayed beyond  $\gamma_{cr}$ , contributing to irregularity in the burst series. The width of the region of coexisting attractors, i.e. the distance  $\gamma_{cr} - \gamma_{sn}$ , ultimately depends on the value of  $\alpha$ : the intersection point between  $\Xi_{min}$  and  $N_u$  exists only if  $\alpha > 4$ , and the increase of  $\alpha$  brings  $\gamma_{cr}$  closer to  $\gamma_{sn}$ . The latter implies that the higher  $\alpha$  is, the more chaotic becomes the bursting: as  $\gamma_{cr} - \gamma_{sn}$  decreases, the burst duration is reduced, making the effects of delay at  $\gamma_{cr}$  more noticeable [10]. In the following, we set  $\alpha = 4.15$ ,

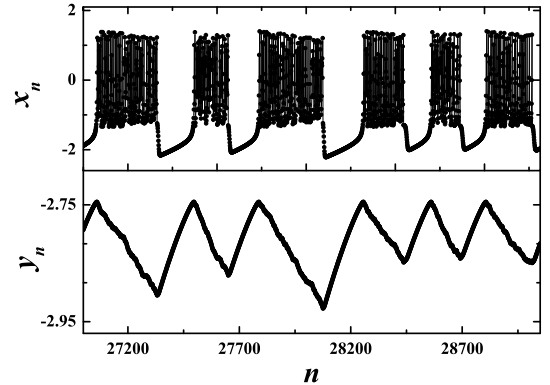


**Fig. 2.** Autonomous dynamics of the Rulkov neuron. For the selected set of map parameters, the fast variable time series (top panel) yields chaotic bursting, whereas the corresponding slow variable waveform (bottom panel) exhibits small amplitude saw-tooth oscillations. The example displayed is obtained for  $\sigma = -0.9$ .

the value already proven to provide a reasonable balance between burst duration and chaoticity [10,12], as demonstrated in Figure 2.

When bursting is enabled ( $\alpha > 4$ ), the neuron activity regime is determined by the position of the slow variable nullcline  $x_n = \sigma$  relative to the parabola vertex. For the small external stimulation, the line  $x_n = \sigma$  crosses  $N_s$ , so that the system remains in a global fixed point, corresponding to the resting state. Evidently, there is a threshold depolarization  $\sigma = \sigma_{th}$ , where the global fixed point loses stability through Neimark-Sacker bifurcation [38],

closely related to the saddle-node bifurcation of the fast subsystem. Above  $\sigma_{th}$ , the slow nullcline intersects  $N_u$ , and the map yields a chaotic series of bursts. The alternation between the periods of bursts and silence rests on the dynamics of the slow variable: whenever the phase point lies above (below)  $x_n = \sigma$ ,  $y_n$  decreases (increases). Finally, let us trace a typical bursting orbit to show hysteresis between the resting and chaotic attractor states. When  $x_n < \sigma$ , the phase point runs  $\mu$ -close to  $N_s$  (inter-burst interval), moving in the direction of  $\gamma$  increase, until  $\gamma_{sn}$  is reached. At  $\gamma_{sn}$ , the onset of bursting is indicated by the potential shooting over  $N_u$ . During the rapid spikes, the potential stays above  $x_n = \sigma$ , driving the slow variable toward  $\gamma_{cr}$ , in whose vicinity the phase point jumps down to  $N_s$ , which results in commencing a new bursting cycle.

## 2.2 Dynamics of the coupled neuron pair

After an overview of an isolated neuron bursting mechanism, let us proceed with the analysis of the dynamics of the two node feedback loop network motif, that constitutes a pair of identical, reciprocally connected neurons. Compared to the previously applied models of chemical synapses, involving coupling either via fast [12,38] or slow variables [11,40], we consider a model that is more general in terms of the form of the threshold function and the inclusion of the time delay. The equations of the interacting neurons are

$$\begin{aligned} x_{i,n+1} &= \frac{\alpha}{1 + x_{i,n}^2} + y_{i,n} - g_c(x_{i,n} - \nu) \\ &\quad \times \frac{1}{1 + \exp(-k(x_{j,n-\tau} - \theta))}, \\ y_{i,n+1} &= y_{i,n} - \mu(x_{i,n} - \sigma), \end{aligned} \quad (2)$$

where the additional indexes  $i, j = 1, 2$  ( $i \neq j$ ) specify the postsynaptic and presynaptic neurons, respectively. The synaptic term, that relates the fast variables, consists of two parts, one of which,  $\frac{1}{1 + \exp(-k(x_{j,n-\tau} - \theta))}$ , describes the action of the presynaptic, and the other,  $g_c(x_{i,n} - \nu)$ , the action of the postsynaptic ionic channels. The former part represents the threshold function, that defines the sharpness of the voltage response of the presynaptic terminals [12]. Formally, the activation threshold is given by  $\theta$ , set to  $\theta = -1.4$ , the value easily reached by the bursting neuron.

The sharpness of the response, or in other words the smearing around the threshold, is determined by the gain parameter  $k$  [22,36,41]. The  $k \gg 1$  case yields the fast threshold modulation model [42], common for the majority of chemical synapses in the brain [34,43], while for  $k \sim 1$  one obtains the more gradual response (graded synaptic transmission model [44]), appropriate for the description of central pattern generators. The time lag  $\tau$  is reflected by the delayed arrival of the presynaptic neuron potential influencing the gating behavior.

Insofar as the postsynaptic part is concerned, the synaptic weight  $g_c$  is related to the maximal conductance

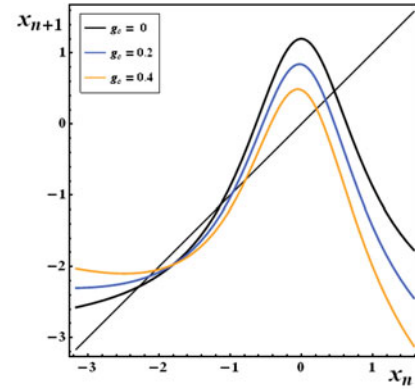


**Fig. 3.** (Color online) First return map of the fast variable at fixed  $y_n = -2.95$ , when the neuron is coupled. Compared to the isolated neuron (black curve), cases  $g_c = 0.2$  and  $g_c = 0.4$ , presented by blue (dark grey) and orange (light grey), respectively, show that increasing the weight reduces the curve's maximum, bringing the middle and right fixed points closer.

of the postsynaptic channels, whereas the reversal potential  $\nu$  determines the excitatory/inhibitory nature of the synapse. In the following,  $\nu$  takes the value  $-1.8$ , giving the inhibitory character to the synapse, as consistent with the ubiquity of the inhibitory pair neuron motif [11,23,45], both in CPGs and other neuron systems.

The dynamical phenomena occurring when coupling is introduced, can be anticipated by examining how the shape of the first return map is affected by the synapse. The genuine correspondence between the maps of the isolated and coupled neurons may only be obtained in case of the sharper synaptic threshold behavior, that is for larger  $k$ . Then the threshold function effectively assumes either value 0 (open synapse) or 1 (closed synapse), reducing the evolution of membrane potential to switches between the maps of the isolated and the coupled neuron. As  $g_c$  is increased, the family of curves (Fig. 3) for the open synapse at an arbitrary  $y_n$  shows ever lesser values of maxima, accounting for the decrease of bursting amplitudes on one hand, and for the middle (in what follows, second) fixed point approaching the right (third), on the other hand. Further, in contrast to the isolated (non-interacting) case, with increasing  $g_c$  at lower boundary values of the available  $y_n$  range, it becomes possible for the map to admit only a single, left (stable) fixed point, as the second and the third fixed point coalesce and eventually disappear through the saddle-node bifurcation.

While we so far addressed the shape of the map at fixed  $y_n$ , a more detailed interpretation of the dynamical phenomena arising through coupling may be obtained by analyzing the nullclines and the curves of the fast variable's maximal and minimal iterates when changing  $y_n$ , in analogy with presented in Figure 1b. It turns out that coupling causes a broader area of phase plane to become accessible to the neuron dynamics, so that its explanation requires the inclusion of the branch of the third fixed point. The specific form of the synapse enables the S-shape of the curves of fixed points, together

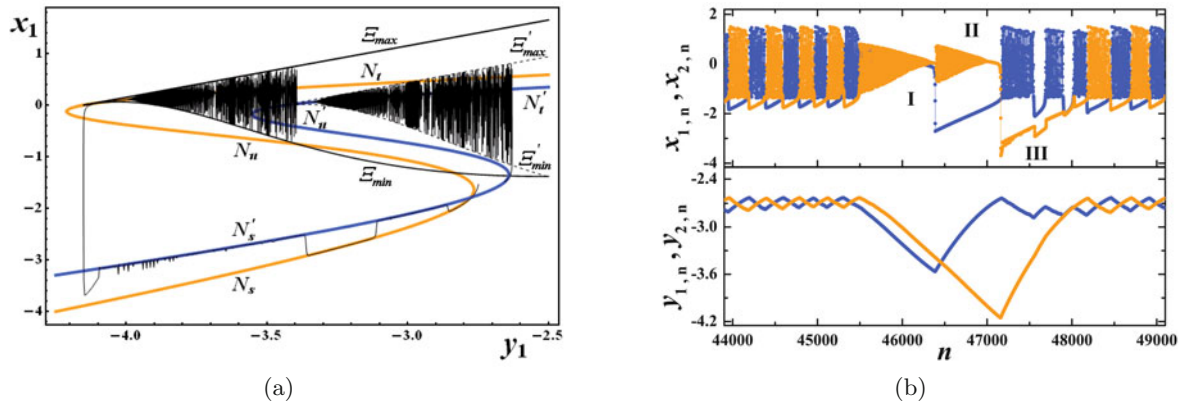


**Fig. 4.** (Color online) (a) Phase plane analysis of the coupled neuron entails the nullclines of all three fast variable fixed points, forming an S-shape curve, be considered. The time series can be explained by the phase point switches between the dynamics determined by the interacting and non-interacting map, whose respective S-curves are displayed with blue (dark grey) and orange (light grey). The branches from top to bottom, obtained for the right, middle and left fixed points, are denoted with  $N_t, N_u$  and  $N_s$  for the isolated map, and the corresponding primed symbols in case of the coupled one. As before, bursting amplitudes are constrained by the curves of minimal and maximal iterates,  $\Xi_{min}$  and  $\Xi_{max}$  (solid black lines), or  $\Xi'_{min}$  and  $\Xi'_{max}$  (dashed black lines). (b) Section of the time series, containing the block sequence (I)–(II)–(III), where the emergent phenomena occur. The top (bottom) panel presents the fast (slow) variable evolution, with blue (dark grey) and orange (light grey) standing for the respective neurons. The orange (light grey) neuron goes through the states corresponding to the common OD (I), partial OD (II) and hyperpolarization (III). The sequence is superimposed in (a) to illustrate the switches between the maps: amplitude reduction in common OD follows the interacting map with  $\Xi'_{min}$  and  $\Xi'_{max}$  as envelopes; partial OD, delimited by  $\Xi_{min}$  and  $\Xi_{max}$ , takes place on the non-interacting map, while during hyperpolarization the phase point turns back to the stable branch  $N'_s$  of the interacting map. The data are obtained for the synaptic parameters  $k = 25, g_c = 0.4, \tau = 10$  and the stimulation current  $\sigma = -0.9$ .

with the belonging stability features, to be maintained, whereas their positions get shifted rightward and upward (see Fig. 4a), compared to the non-interacting case. In parallel, the  $x$ -coordinate of the left knee of the S-curve, where the branches of the unstable  $N'_u$  (the primed symbols denote the curves related to the interacting, i.e. shifted map) and the third fixed point  $N'_t$  meet, remains approximately the same as for the isolated neuron. Also, one may numerically evaluate the curves of minimal  $\Xi'_{min}$  and maximal iterates  $\Xi'_{max}$ , that no longer present the first and second image of zero, whereby the important difference to the non-interacting case lies in the lack of intersection between the curve  $\Xi'_{min}$  and the branch of the unstable fixed points  $N'_u$ . Precisely the latter may be directly related to the occurrence of the emergent phenomena, understood as the dynamical phenomena that cannot be readily predicted from the action of the isolated neuron.

To take an example of such phenomena, let us analyze the sequence (I)–(II)–(III) of the neuron displayed in orange (light grey) in Figure 4b, where, by the order of appearance, common OD, partial OD [32,46] and the hyperpolarization of membrane potential may be recognized. The two former relate to suppression of the amplitude of the membrane potential, whereas the third corresponds to lying in states whose potential is lower than that of the resting level. The mechanism of how the above sequence emerges, as demonstrated in Figure 4a, is characterized by remaining on and switching between the isolated and cou-

pled maps. Amplitude suppression preceding the common OD (I) unfolds by the map of the coupled neuron between the curves  $\Xi'_{min}$  and  $\Xi'_{max}$ , ending, after a chaotic transient, in a cascade of inverse Hopf bifurcations. OD itself corresponds to a sequence of slowly drifting depolarized states that trace the orbit along the branch of the third fixed point  $N'_t$  near the intersection between  $\Xi'_{min}$  and  $\Xi'_{max}$ , approaching the left knee of the S-curve. The suppression sequence before the partial OD (II) is induced by the transition from the map of the coupled to the map of isolated neuron, since the potential of the other neuron at the resting state lies lower than the synaptic activation threshold  $\theta$ . With the  $y$ -coordinate of the left knee of the S-curve outside the interval between the external crises of the isolated map, the observed neuron goes through the sequence of inverse Hopf bifurcations, similar to the one on the coupled map, getting closer to the isolated map's left knee. By residing in partial OD, an area of phase plane with small values of the slow variable becomes accessible to the neuron dynamics, so that such phenomena are reflected in the absolute minima of the slow variable time series. The transition to hyperpolarized state (III) coincides with the jump from the branch of the third fixed point  $N'_t$  of the isolated map to the stable branch  $N'_s$  of the coupled map. This is induced by the other neuron exceeding the synaptic activation threshold  $\theta$ , whereby the rate of the transition to the coupled map shows minor dependence on  $k$  and  $\tau$ .

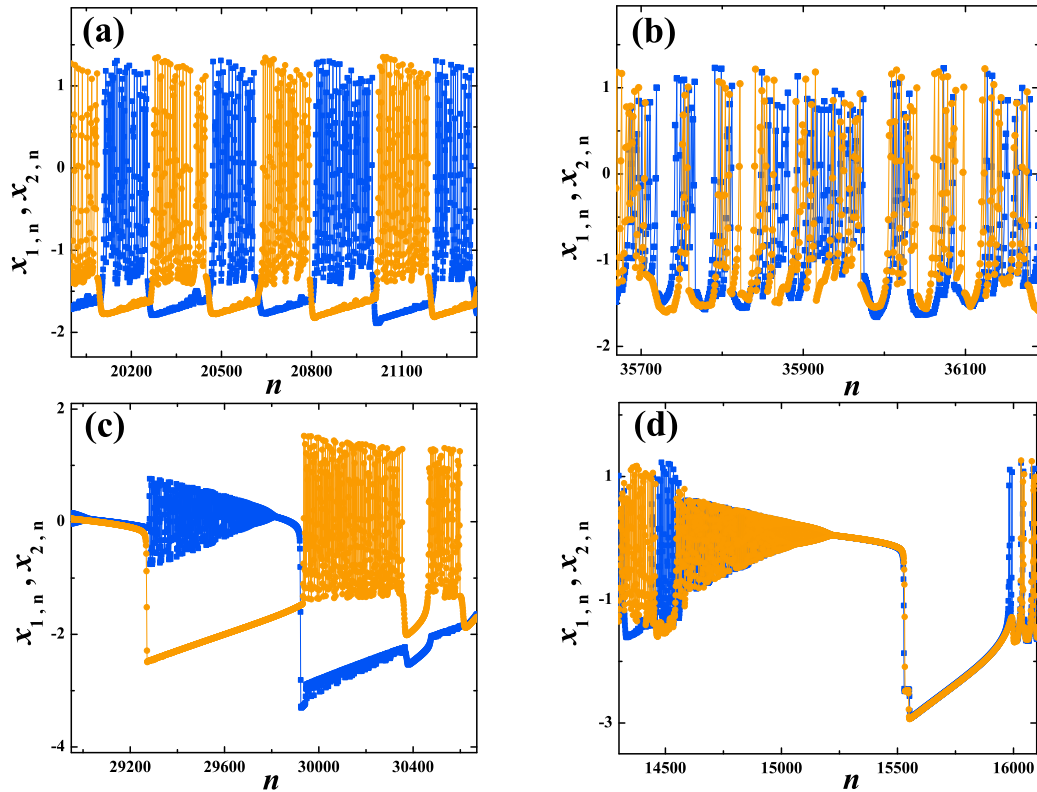


**Fig. 5.** (Color online) Characteristic sequences making up the time series of the coupled neurons, with the fast variable waveforms represented by blue (dark grey) and orange (light grey). (a) Chaotic anti-phase burst synchronization is a common form of neuron collective behavior. (b) Chaotic phase burst synchronization arises for intermediate  $g_c$  and low  $k$  values. (c) Block sequence containing the partial OD and the membrane potential hyperpolarization. While the blue (dark grey) neuron goes through amplitude suppression superseded by the hyperpolarized states, the orange (light grey) neuron lies in the quasi-stable resting state, followed by bursting. (d) Block sequence containing the common OD and the prolonged quiescence.

Apart from the emergent phenomena, the switches between the maps present the basis to explain the more common regimes of cooperative behavior, including the anti-phase and phase burst synchronization. For example, in the former case, the alternation between the sequences of bursting and resting for neuron 1 coincides with its phase point transition from the isolated to the coupled map. Namely, bursting follows the non-interacting map, because the potential of the other neuron, say neuron 2, lies below  $\theta$ . Complementary, the increase of potential on neuron 1 during resting corresponds to the phase point moving along the stable branch of the coupled map up until its right knee is reached, while neuron 2 is at bursting, with the envelopes determined by  $\Xi_{min}$  and  $\Xi_{max}$  of the non-interacting map. This mechanism is enabled by the position of the isolated map relative to the coupled one, provided that the curve  $\Xi_{min}$  lies above  $\theta$ .

### 2.3 Analysis of synchronization between chaotic neuron time series

After the detailed analysis of the phase plane dynamics, we address qualitatively the sequences within the time series, in view of the fact that their overlaps can be related

to the different regimes, where intermittent synchronization is achieved. As with the models applying the simpler form of synapse, the anti-phase chaotic burst synchronization (Fig. 5a) here also stands out as the primary type of synchronization at small  $g_c$ . For small  $k$ , at intermediate  $g_c$  and higher  $\sigma$ , one finds the mentioned regime in coexistence with phase burst synchronization (Fig. 5b). With increasing  $g_c$ , the synchronization regimes may also be influenced by the growing number of states, resulting from the emergent phenomena, that include partial (see Fig. 5c) and common OD (see Fig. 5d), hyperpolarization of membrane potential and the prolonged quiescence. Observing the time series, one finds the emergent phenomena to occur in block sequences (sequences linked in specific order), so that the hyperpolarization can only follow the partial OD, whereas the prolonged quiescence comes after the common OD. The OD phenomena, the partial or the common ones, encompass the suppression of the neuron potential amplitude, leaving one or both neurons simultaneously in the non-spiking depolarized state. The common OD is preceded by the amplitude reduction sequence, that begins by one of the neurons bursting, and the other exceeding  $\theta$ . There is a twofold scenario of leaving the common OD: by one, both of the neurons go to the prolonged quiescence, and by the other, partial OD occurs. Applying

the phase plane analysis analogous to the one presented in Section 2.2, we established that the realization of the scenarios is related to the value of  $\tau$ : the larger  $\tau$  becomes, the joint transition to prolonged quiescence is more likely to prevail. Namely, at higher  $\tau$ , the closing of the synapse is delayed as a consequence of the membrane potentials of both of the neurons following the coupled map. In a broader perspective, the emergence of OD has been related, apart from the heterogeneity in the oscillator parameters, to the specific properties of the coupling between the identical oscillators [47]. The above mentioned dependence on  $\tau$  and the analysis from Section 2.2 suggest that the applied model exhibits the interplay between the two such effects: the dynamical coupling [48] and the synaptic time delay [49,50].

Due to frequent occurrence of the emergent phenomena, resulting in the states considered, in order to quantify synchronization one cannot introduce a proper phase variable in the sense of [39], where the nearly periodic, small amplitude saw-tooth oscillations of the slow variable were used. The observed complexity of the time series requires that the understanding of synchronization be adapted so as to encompass the overlaps between the simultaneous states of the neurons' fast variables. Considering Figure 5, one infers synchronization conceived in this fashion to be contributed by the sequences of time series presented in Figures 5b and 5d. In particular, in Figure 5b, there is an overlap between the bursts, whereas in Figure 5d the overlap occurs during the sequences of amplitude suppression and prolonged quiescence. Loosely speaking, the former may be viewed as the "temporary" chaotic burst synchronization, and the latter as the "temporary" exact synchronization.

Since within the time series the described sequences may repeat a different number of times and with varying duration, it is convenient to introduce the parameter that characterizes the matching between the time courses of the fast variables. First, we define the average value of the neuron fast variables at the iteration step  $n$ ,  $\bar{x}_n = \frac{1}{2}(x_{1,n} + x_{2,n})$ , so that its course coincides with one of the variables in the case of complete synchronization. Then it is suitable to consider the quantity  $R$ , already seen useful in [51,52], given by:

$$R_{x_1, x_2} = \frac{[\langle \bar{x}_n^2 \rangle] - [\langle \bar{x}_n \rangle^2]}{\frac{1}{2} \sum_{i=1}^2 ([\langle x_{i,n}^2 \rangle] - [\langle x_{i,n} \rangle^2])}, \quad (3)$$

where the angled brackets denote averages over long time series of  $n_{max} = 50\,000$  map iterations, and the squared brackets refer to averaging over an ensemble of 200 trials with different initial conditions.  $R_{x_1, x_2}$  may be viewed as an appropriate numerical tool, since we confirmed its value to remain approximately constant if the number of trials is increased. As stated previously, by comparing the fast variable time series of the two neurons, one may observe the overlaps in finite time intervals, that correspond to sequences comprising intermittent synchronization. Within this context,  $R$  is used to quantify the cumulative contribution of such regimes, assuming values in the range from

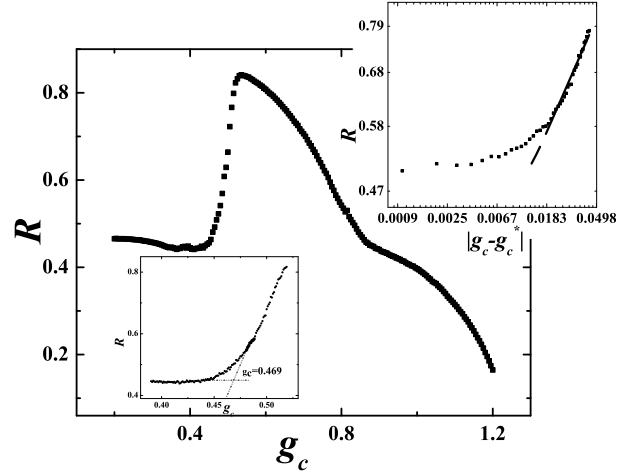


**Fig. 6.**  $R$  plot against  $g_c$  for  $k = 10$ ,  $\tau = 5$  and  $\sigma = -0.6$ . The lower inset displays the enhanced region of  $R$  sudden increase, with  $g_c^*$  determined in such a way as to correct for the dulling of  $R$ . The larger  $k$ , the less expressed is the rounding effect. The upper inset,  $R$  vs.  $g_c - g_c^*$  on the log-log scale, shows how the scaling exponent  $\kappa_g$  is calculated.

0 to 1, where the upper boundary would correspond to the case of completely synchronized series. Evidently,  $R$  does not pose a universal measure of synchronization, but is adapted to the system at hand, and can be viewed in a broader spectrum of synchronization measures among chaotic systems, e.g. correlation and others [53–55].

### 3 Results

We study how the quantity  $R$  depends on  $g_c$  when changing the parameters  $k, \sigma$  and  $\tau$ . The shape of  $R$  is most significantly altered by varying  $\sigma$ , and the segment with the sudden rise sets in only if  $\sigma > \sigma_c = -1.05$ , where the function  $\sigma_c(k, \tau)$  remains approximately constant. In Figure 6  $R(g_c)$  shows three characteristic intervals: the regime with slowly varying  $R$ , the regime of sudden rise at the narrow  $g_c$  interval and the regime of monotonous decline. The scope is on the transition between the first and second regime at the intermediate values of  $g_c$ .

At the onset of the sudden rise determined by  $g_c^*$ , we find that  $R$  scales as a power law

$$R \sim (g_c - g_c^*)^{\kappa_g}, \quad (4)$$

where  $\kappa_g$  takes the role of the scaling exponent (see the inset of Fig. 6). The similar behavior has already been established in systems of coupled phase oscillators [39,56]. An analogous scaling relation for  $R(\sigma)$  at fixed  $g_c$  will be considered in Section 3.4.

#### 3.1 The effects of the time delay $\tau$ variation on the form of $R(g_c)$

We investigate how the nonlinear dependence  $R(g_c)$  is affected by the increase of  $\tau$ . In the vicinity of  $g_c^*$ , the  $R$

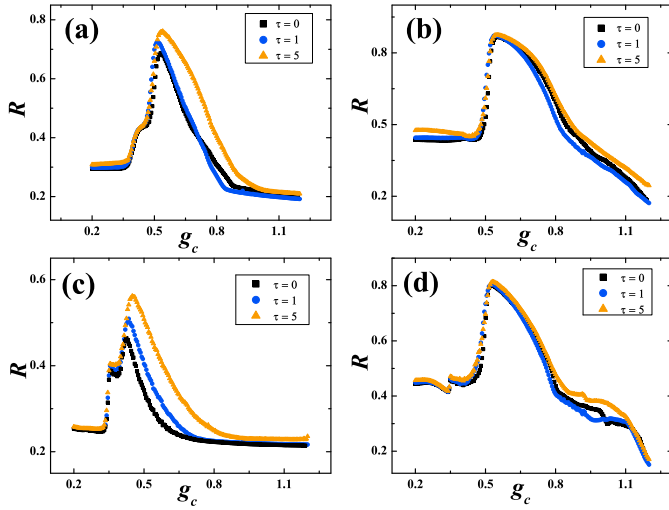


**Fig. 7.** (Color online)  $R(g_c)$  family of curves under variation of  $\tau$ , with black, blue (dark grey) and orange (light grey) lines representing  $\tau = 0, 1$  and  $5$ , respectively. The upper row is obtained for  $k = 5$ , and the lower row for  $k = 25$ . Two values of  $\sigma$  are presented:  $\sigma = -0.9$  (left column, note the two knees) and  $\sigma = -0.6$  (right column). It is evident that  $\kappa_g$  dependence on  $\tau$  is negligible.

families of curves in Figure 7 show little change with  $\tau$ , meaning that  $\tau$  does not alter the  $\kappa_g$  value significantly. For instance, in the case  $k = 25$  and  $\sigma = -0.6$ , we obtain  $\kappa_g = 0.33(1)$  at  $\tau = 0$ ,  $\kappa_g = 0.36(1)$  at  $\tau = 5$  (in units of iteration steps) and  $\kappa_g = 0.34(1)$  at  $\tau = 10$ .

Even so, one may identify an area of phase space confined to  $-0.9 \lesssim \sigma \lesssim -0.75$ , where  $\tau$  especially favors the increase of maximum value  $R_{max}$  of the particular  $R(g_c)$  curves, whereas the weights  $g_{c,max}$  corresponding to  $R_{max}$  show the largest variation with  $k$ , reducing when it is increased. Changing  $k$  also has an effect on the very form of the  $R_{max}(\tau)$  dependence, as displayed for the families of curves  $R_{max}(\tau)$  over  $\sigma$  in the cases  $k = 5$  (Fig. 8a) and  $k = 25$  (Fig. 8b). Only for small  $\sigma$ , there is an obvious peak at the characteristic time delay  $\tau^*$ , that is shifted to higher values with  $k$ , e.g. from  $\tau^*(\sigma = -0.9, k = 5) = 5$  to  $\tau^*(\sigma = -0.9, k = 25) = 17$ . Enhancing  $\sigma$  for an arbitrary  $k$ , the bottom-to-top order in which the pertaining curves appear is preserved, so that the value of  $R_{max}$  at fixed  $\tau$  rises.

Comparing Figures 7a and 7c, for  $\sigma = -0.9$ , with Figures 7b and 7d, for  $\sigma = -0.6$ , one may notice another important difference in behavior of  $R(g_c)$  under variation of  $\sigma$ . Namely, when increasing  $g_c$  for moderate values of  $\sigma$ , two knees may be observed, while for  $\sigma \approx -0.6$ , one obtains the  $R$  curve with only a single knee. Moreover, the transition between the two forms of behavior appears to be continuous. With rising  $\sigma$ , the plateaus before the first and the second knee level each other out, which ultimately leads to the first knee disappearing. This may also be confirmed by the observed similarity of  $\kappa_g$  values for  $\sigma = -0.9$  at the second knee and for  $\sigma = -0.6$  at the single knee. To illustrate this, we cite the ob-

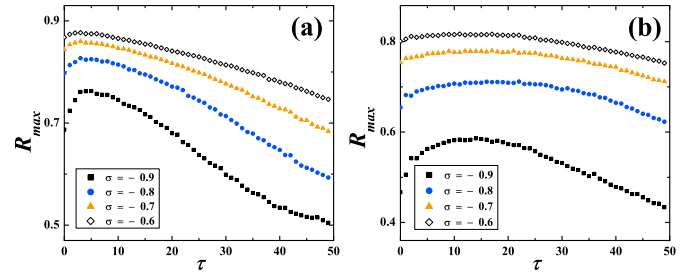


**Fig. 8.** (Color online)  $R_{max}(\tau)$  family of curves under variation of  $\sigma$ , with black, blue (dark grey), orange (light grey) and empty symbols representing the cases  $\sigma = -0.9, -0.8, -0.7$  and  $-0.6$ , respectively. (a)  $k = 5$ : at small  $\sigma$ , there is an obvious peak at  $\tau^* = 5$ , and the flatter curves for increasing  $\sigma$  show the rise of  $R_{max}$  at an arbitrary  $\tau$ ; (b)  $k = 25$ : the bottom-to-top order of curves remains identical to the one for  $k = 5$ , but the maximum values shift to  $\tau^* = 17$ .

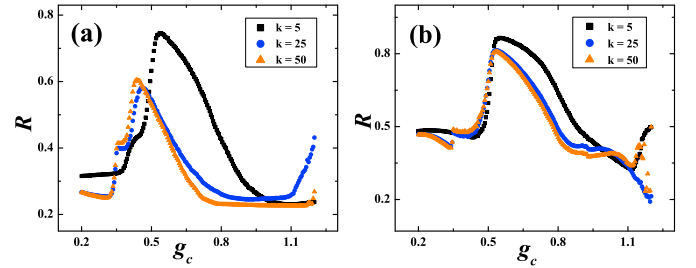


**Fig. 9.** (Color online)  $R(g_c)$  family of curves under variation of  $k$  at fixed  $\tau = 10$ , with black, blue (dark grey) and orange (light grey) symbols representing  $k = 5, 25$  and  $50$ , respectively. (a)  $\sigma = -0.9$ : at moderate stimulation, there is the  $k$  value, above which the curves tend to the unique limiting form; (b)  $\sigma = -0.6$ : at strong stimulation, different synaptic threshold models (small  $k$  as opposed to large  $k$ ) are not clearly distinguishable.

tained values  $\kappa_g(k = 25, \tau = 5, \sigma = -0.6) = 0.36(1)$  and  $\kappa_g(k = 25, \tau = 5, \sigma = -0.9) = 0.35(2)$ .

### 3.2 Dependence of $R(g_c)$ on the synaptic gain parameter $k$

The single- and double-knee types of  $R(g_c)$  behavior may additionally be distinguished if varying  $k$  (Fig. 9). Enhancing  $k$ , the  $R(g_c)$  curves asymptotically tend to the form that they would assume if the Heaviside threshold function (case  $k \rightarrow \infty$ ) were applied to model the chemical synapse. We note that for  $\sigma = -0.6$ , the value of  $\kappa_g$  exponent (see Tab. 1) is not dependent on  $k$ , e.g. at  $\tau = 5$  one obtains:  $\kappa_g(k = 5) = 0.34(1)$ ,  $\kappa_g(k = 10) = 0.36(1)$  and  $\kappa_g(k = 25) = 0.36(1)$ . By way of contrast, for  $\sigma = -0.9$ , the exponent values at the first and second knees, where  $\kappa_{g1} \neq \kappa_{g2}$  holds, change with increasing  $k$ . Accordingly, at  $\tau = 5$ , we get  $\kappa_{g1}(k = 5) = 0.13(1)$  and  $\kappa_{g2}(k = 5) = 0.29(1)$ , while for larger  $k$ ,  $\kappa_{g1}(k = 10) = 0.26(1)$  and  $\kappa_{g2}(k = 10) = 0.19(1)$ . Particularly interesting is the fact that the characteristic value  $k^* \approx 9$  may be found, at

**Table 1.**  $\kappa_g$  exponent values obtained for the  $R(g_c)$  power-law behavior under variation of  $k$  and  $\sigma$  at fixed  $\tau = 5$ . The pairs of values displayed for  $\sigma = -0.9$  result from the double-knee  $R(g_c)$  curves, like the ones in Figure 9a.

$k$		5	10	25
$\sigma = -0.6$		0.34(1)	0.36(1)	0.36(1)
$\sigma = -0.9$	1st knee	0.13(1)	0.26(1)	0.30(1)
	2nd knee	0.29(1)	0.19(1)	0.18(1)

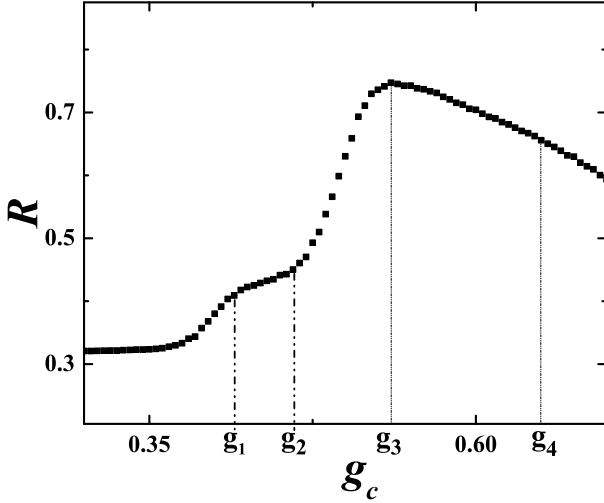


**Fig. 10.** Two knees graph of  $R(g_c)$  for  $k = 5$ ,  $\tau = 10$  and  $\sigma = -0.9$ . The four  $g_c$  values ( $g_1 = 0.417$ ,  $g_2 = 0.469$ ,  $g_3 = 0.538$  and  $g_4 = 0.65$ ), are singled out to distinguish between the four characteristics segments of  $R(g_c)$ : the first knee, plateau, the second knee and the monotonous decay.

which the second knee exponent supersedes the exponent at the first knee (to be analyzed elsewhere).

For  $k > k^*$ ,  $\kappa_{g_1}$  assumes approximately the constant value, no matter how  $k$  is increased, indicating it to be the value one would obtain in the case of the Heaviside threshold function. As an illustration, at  $\tau = 5$ , for the set  $k = 10, 13, 25$  the scaling exponents we find are  $\kappa_{g_1} = 0.26(1)$ ,  $\kappa_{g_1} = 0.28(1)$  and  $\kappa_{g_1} = 0.30(1)$ , respectively. Arguably,  $k^*$  may be interpreted as the value of  $k$  at the boundary between the graded synaptic transmission and the threshold modulation synaptic models.

### 3.3 An insight into the transient states behind the form of $R(g_c)$

We investigate in detail the dynamical mechanisms responsible for the shape of  $R(g_c)$ , focusing on the graphs with two knees at  $\sigma = -0.9$ . Here we present the analysis for the generic case  $k = 5$  and  $\tau = 10$ , whereas larger  $k$  would result in the plateau before the second knee becoming even less inclined.

In the graph  $R(g_c)$  (Fig. 10), we single out the four characteristic values of  $g_c$  that correspond to plateau boundaries ( $g_1, g_2$ ), maximum value of  $R(g_c = g_3)$ , and one of the points on the declining section of the curve

$R(g_c = g_4)$ . Increasing  $g_c$  up to  $g_1$ ,  $R$  grows due to the occurrence of simultaneous entries to OD, corresponding to the amplitude suppression. The ODs do not end by the two neurons undergoing common transition to the resting state (RS), as the common ODs appear only in sequences, superseded by the partial ones. The scenario of leaving the partial OD consists in passing to the hyperpolarized state (HS), whose potential is lower than the RS. Along with ODs, the increase of  $R$  up to  $g_1$  is also contributed by the phase slips [12,39], that bring about the accidental overlaps between membrane potentials of the two neurons during bursting. Effect of phase slips, directly related to strength of the inhibitory synapse, considerably decreases with the increase of  $g_c$ .

Above  $g_c = g_1$ , the synaptic strength is sufficient to reduce the number of slips and to cause the simultaneous rise in number of ODs, both the common and the partial ones. However, while at  $g_1$  the common oscillation death is always succeeded by the partial one, at  $g_2$  the ODs after which both of the neurons settle at the RS begin to emerge.

In the  $g_2$  to  $g_3$  interval, the number of ODs remains approximately unchanged, yet more of them end with the joint transition to the RS, contributing to the increase of  $R$ . At  $g_3$ , the occurrence of ODs is further regularized, while HS caused by the partial OD disappear. The decline of  $R$  for  $g_c > g_3$  may be explained by the rising level of the resting potential, whereas the number and structure of ODs is unaltered.

The mechanism behind the  $R(g_c)$  dependence may be clarified by analyzing the orbits of two neurons in the phase space, that is for simplicity split into the subspaces of fast and slow variables. The four panels in Figure 11 are presented at characteristic values of synaptic weights  $g_1, g_2, g_3$  and  $g_4$ , respectively. In the panel A on the left, the wings of the graph correspond to the regime of the anti-phase burst synchronization, while the points left and below the wings represent the sequences of inverse Hopf bifurcation prior to partial OD. The small value of  $R(g_1)$  is related to the low number of points along the main diagonal, with the values of fast variables around zero reflecting the depolarized states of ODs, and the points close to the main diagonal representing the sequences of decreasing oscillation amplitudes before the entry to OD.

At the end of the plateau, for  $g_c = g_2$ , one may observe the balancing of the two effects. The decrease of the number of points between the wings and the OD sequences is the consequence of the phase slips vanishing, and the appearance of points along the main diagonal below the wings is caused by the common transitions to the RS when both of the neurons escape the OD.

Alternatively, it is convenient to interpret the described processes by observing their counterparts in the slow variables subspace. Tracing the orbit around and above the main diagonal in the clockwise direction, we infer the part of decreasing  $y_1$  and  $y_2$  to correspond to the sequence of diminishing potential amplitudes and the common transitions to OD. The wing where  $y_1$  decreases reflects the regime of partial OD, whereby the first

neuron ceases to oscillate, while the other is at the RS. The wing at increasing  $y_1$  corresponds to the regime of the first neuron hyperpolarization, with the other neuron evolving through the series of states bursting  $\rightarrow$  resting  $\rightarrow$  bursting, whose succession is marked by breaking points of the trajectory in the slow variable subspace.

For  $g_c = g_3$ , the cessation of partial ODs is reflected by the disappearance of the points left and below the wings in the subspace of the fast variables, accompanied by the orbits of slow variables contracting along the main diagonal. We note that the section of the orbit with decreasing  $y_1$  and  $y_2$  is linked to the regime of common ODs, whereas the section of the orbit at their increase is tied to the anti-phase coordinated bursting.

The decline of  $R$  above  $g_3$  may be related to the rising level of the RS, leading to the effective reduction of the shared time spent at the RS after OD. In addition, the orbits in slow variables subspace expand off the main diagonal, which is likely to account for the appearance of amplitude modulated bursting and the slightly modified approach to OD.

### 3.4 Scaling law with the external bias current $\sigma$

Along with the scaling of  $R(g_c)$  at fixed  $\sigma$ , we also find the empirical scaling law at the sudden rise of  $R(\sigma)$  at fixed  $g_c$ :

$$R(\sigma) \sim (\sigma - \sigma^*)^{\kappa_\sigma}, \quad (5)$$

where  $\kappa_\sigma$  denotes the scaling exponent, and  $\sigma^*$  represents the external bias current at the onset of synchronization increase (Fig. 12a).

The  $\kappa_\sigma$  value primarily depends on  $g_c$  (see Fig. 12b), with the increase of  $g_c$  causing  $\kappa_\sigma$  to change very little with  $k$  and  $\tau$  (see Tab. 2). As with  $\kappa_g$ , we find  $\kappa_\sigma$  to display only marginal dependence on  $\tau$  (see Fig. 12c). In agreement with the nonlinear form of  $R(g_c)$ , one might expect  $\kappa_\sigma$  at the vicinity of  $g_c = 0.5$  (provided  $k$  fixed) to display largest variation with  $\tau$  (Tab. 2).

Another way to distinguish between the models of graded synaptic transmission and fast threshold modulation chemical synapses can be found by observing  $\kappa_\sigma(k)$  dependence. In Figure 12d, cases of small and large  $k$  differ in so far as the curves at moderate and high  $k$  approach the common asymptotic form. The suspected threshold model difference may be verified by surveying Table 2, that implies  $\kappa_\sigma(g_c)$  to be a weak function for the fast modulation model. If one recalls the  $R(g_c)$  family of curves under variation of  $k$  (Fig. 9a) to compare it with the family in Figure 12d, it strikes that for the graded synapse both smaller  $g_c^*$  and  $\sigma^*$  are sufficient to induce the sharp increase of  $R$ .

## 4 Summary

We have considered the inhibitory motif consisting of two identical, reciprocally coupled neurons, whose dynamics follows the chaotic Rulkov map, with the parameters selected to set the neurons into the bursting regime. The

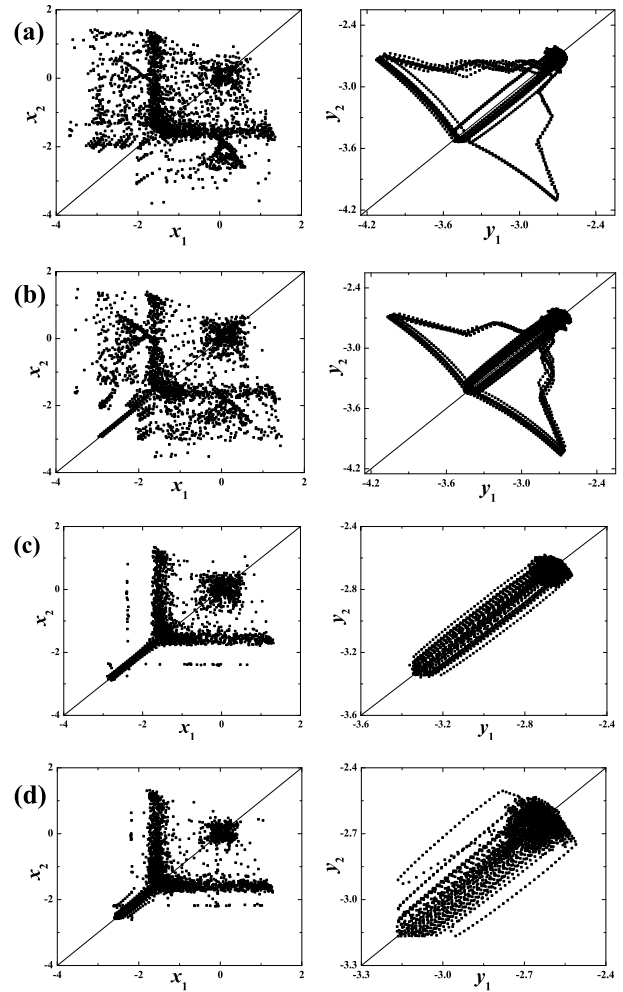


**Fig. 11.** Phase portraits in the subspaces of fast (left column) and slow (right column) variables at four characteristic  $g_c$  values:  $g_1 = 0.417$  (row (a)),  $g_2 = 0.469$  (row (b)),  $g_3 = 0.538$  (row (c)) and  $g_4 = 0.65$  (row (d)), with  $k = 5$ ,  $\tau = 10$  and  $\sigma = -0.9$  fixed.

adopted model of chemical synapse involves a threshold function, such that its gain parameter  $k$  modifies the sharpness of the voltage response, enabling one to study the behavior similar to fast threshold modulation (case  $k \gg 1$ ), as well as graded synaptic transmission ( $k \sim 1$ ). The time lag  $\tau$  is taken into account by assuming that the opening of the synapse is influenced by whether the presynaptic membrane potential, delayed by  $\tau$ , exceeds the activation threshold  $\theta$ .

Building on the phase plane analysis of an isolated (noninteracting) neuron map, we obtain analytically how the fast nullclines and the curves of minimal and maximal iterates get shifted rightward and upward under the action of the synapse. Such an approach enabled us to trace, for the first time, the time series of the coupled neurons back to the motion of the phase point, whose orbits are determined by the noninteracting and interacting maps and the switches between them. As a specific coupling effect, we find that a larger area of phase plane becomes available to the neuron dynamics. This results in the emergent

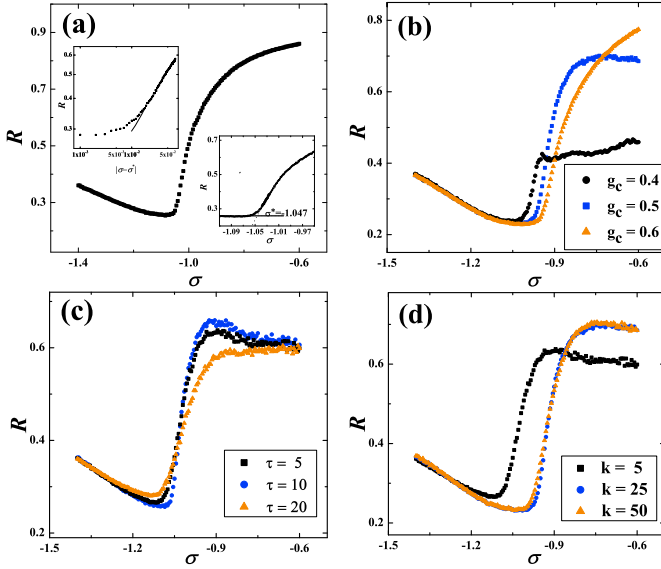


**Fig. 12.** (Color online) Quantity  $R$  dependence on  $\sigma$ . (a) An example of sudden increase of  $R$ , with the onset of synchronization at  $\sigma^*$  (lower inset) and the scaling exponent  $\kappa_\sigma$  (upper inset), for  $k = 5, \tau = 5$  and  $g_c = 0.6$ . (b)  $R(\sigma)$  family at  $k = 5$  and  $\tau = 10$  under variation of  $g_c$ , with  $g_c = 0.4, g_c = 0.5$  and  $g_c = 0.6$  represented by black, blue (dark grey) and orange (light grey) symbols, respectively. (c)  $R(\sigma)$  family at  $k = 5$  and  $g_c = 0.5$  for varying  $\tau$ , with  $\tau = 5, \tau = 10$  and  $\tau = 20$  represented by black, blue (dark grey) and orange (light grey) symbols, respectively. (d)  $R(\sigma)$  family with varying  $k$  ( $\tau = 10$  and  $g_c = 0.5$  fixed): cases  $k = 5, 25$  and  $50$  are displayed by black, blue (dark grey) and orange (light grey) symbols, respectively.

**Table 2.**  $\kappa_\sigma$  exponent values, following  $R(\sigma)$  power-law behavior, for fixed  $\tau = 10$  and varying  $k$  and  $g_c$ .

$g_c$	0.4	0.5	0.6
$k = 5$	0.16(1)	0.30(1)	0.31(1)
$k = 25$	0.30(1)	0.45(1)	0.36(1)

phenomena of partial and common OD, membrane potential hyperpolarization and the prolonged quiescence, manifesting in several block sequences through the time series. For some of the observed phenomena analogs may be found when the more realistic neuron models are applied. These include the transitions to OD from spiking (observed on coupled Hodgkin-Huxley neurons in [34], also for the so-called spike death [57]) or from bursting (Hindmarsh-Rose model [36]) regime, as well as the phenomena of firing death [58], and even the population death (Fitzhugh-Nagumo model [59]). Though the transient oscillation death has been indicated in the time series of the Hodgkin-Huxley neuron pair [60], the waveforms reported here show the greatest resemblance to those on coupled Hindmarsh-Rose neurons [36,61,62]. This relates, among others, to the depolarized states corresponding to OD, but also to the general appearance of the bursting sequences.

Bearing in mind that the occurrence of the emergent phenomena results in the complex time series of the motif's neurons, among which no asymptotically stable syn-

chronization regime can be established, one is required to extend the understanding of synchronization so as to encompass the intermittent overlaps between the sequences within the time series. To do so, it is convenient to introduce the quantity  $R$ , that amounts to the cumulative contribution of all the overlapping sequences. Taking averages over the sufficiently long time series and the set of different initial conditions makes it appropriate to use  $R$  to characterize the dependence of the degree of synchronization on the neuron and synaptic parameters. In particular, we identify the intervals of both  $\sigma$  and  $g_c$  corresponding to the sudden rise of  $R$ , such that its onset obeys a power law.

As  $\sigma$  is varied, the dependence  $R(g_c)$  can exhibit one or two knees. For the latter, the increase of  $R$  at the first knee occurs due to the overlaps in the block sequences of partial ODs (presented in Fig. 4b), and the rise at the second knee coincides with the overlaps appearing during the common OD and the prolonged quiescence (Fig. 5d). The distribution of the encountered block sequences is found to depend on  $k$  and  $\tau$ . We show that the different threshold models of synaptic behavior-graded synaptic transmission as opposed to fast threshold modulation, typify two classes of families of curves  $R(g_c)$  and  $R(\sigma)$ , as reflected by the corresponding values of the scaling exponents. The preliminary results on systems with a larger number of neurons indicate that the shape of the  $R(g_c)$  curves with two knees, accompanied by the scaling laws, is generic, though the level of the second knee is higher than in case of two neurons, as it becomes increasingly difficult to achieve common oscillation death. In a larger population, it may be possible to relate the existence of partial ODs to the formation of functional subassemblies, consisting of transiently synchronized neurons [38,40,63,64]. Also, in reference to the preliminary results on larger systems, the existence of the scaling law may be viewed in context of the systems of coupled oscillators, where the similar laws, observed at the onset of synchronization, are considered a signature of the second order phase transitions. Such phase transitions to synchronization have first been observed in systems of globally (mean field) coupled phase oscillators [56], and in systems of bursting neurons [13,39] at the later stage. In addition, it has recently been shown that the transitions to synchronization exist for a broader class of oscillators [65]. From another perspective, the double occurrence of the scaling law when coupling is increased, has been reported in systems of coupled oscillators [66] exhibiting successive second order phase transitions, first to partial, and then to common OD. Looking ahead, pursuing the research on the present and improved models of neuron maps could yet prove interesting not only for understanding the interaction mechanisms of bursting neurons, but may also offer a promising outlook into different forms of collective behavior in a broader class of coupled dynamical systems.

This research was performed as part of the work within project No.141020, funded by the Serbian Ministry of Science and Technological Development.

## References

1. R. Milo, S. Shen-Orr, S. Itzkovitz, N. Kashtan, D. Chklovskii, U. Alon, *Science* **298**, 824 (2002)
2. U. Alon, *Nature* **8**, 450 (2007)
3. O. Sporns, R. Kotter, *PLoS Biol.* **2**, e369 (2004)
4. S. Song, P.J. Sjoström, M. Reigl, S. Nelson, D.B. Chklovskii, *PLoS Biol.* **3**, e68 (2005)
5. E. Bullmore, O. Sporns, *Nature* **10**, 186 (2009)
6. R.J. Prill, P.A. Iglesias, A. Levchenko, *PLoS Biol.* **3**, e343 (2005)
7. C. Li, *Phys. Rev. E* **78**, 037101 (2008)
8. R.C. Elson, A.I. Selverston, R. Huerta, N.F. Rulkov, M.I. Rabinovich, H.D.I. Abarbanel, *Phys. Rev. Lett.* **81**, 25 (1998)
9. R.C. Elson, A.I. Selverston, H.D.I. Abarbanel, M.I. Rabinovich, *J. Neurophysiol.* **88**, 1166 (2002)
10. G. de Vries, *Phys. Rev. E* **64**, 051914 (2001)
11. B. Ibarz, J.S. Casado, M.A.F. Sanjuán, *Phys. Rev. E* **75**, 041911 (2007)
12. B. Ibarz, H. Cao, M.A.F. Sanjuán, *Phys. Rev. E* **77**, 051918 (2008)
13. M.V. Ivanchenko, G.V. Osipov, V.D. Shalfeev, J. Kurths, *Phys. Rev. Lett.* **93**, 134101 (2004)
14. S.K. Han, D.E. Postnov, *Chaos* **13**, 1105 (2003)
15. L.M. Pecora, T.L. Carroll, *Phys. Rev. Lett.* **64**, 821 (1990)
16. H.D.I. Abarbanel, N.F. Rulkov, M.M. Sushchik, *Phys. Rev. E* **53**, 4528 (1996)
17. M.G. Rosenblum, A.S. Pikovsky, J. Kurths, *Phys. Rev. Lett.* **76**, 1804 (1996)
18. L. Zhao, Y.-C. Lai, C.-W. Shih, *Phys. Rev. E* **72**, 036212 (2005)
19. S. Rajesh, S. Sinha, S. Sinha, *Phys. Rev. E* **75**, 011906 (2007)
20. G.L. Baker, J.A. Blackburn, H.J.T. Smith, *Phys. Rev. Lett.* **81**, 554 (1998)
21. M.G. Rosenblum, A.S. Pikovsky, J. Kurths, *Phys. Rev. Lett.* **78**, 4193 (1997)
22. I. Belykh, E. de Lange, M. Hasler, *Phys. Rev. Lett.* **94**, 188101 (2005)
23. A. Shilnikov, R. Gordon, I. Belykh, *Chaos* **18**, 037120 (2008)
24. L. Schimansky-Geier, V.S. Anishchenko, A. Neiman in *Neuro-informatics and neural modelling*, edited by F. Moss, S. Gielen (Elsevier, Amsterdam, 2001), p. 23
25. J. Rinzel, in *Mathematical topics in population biology, morphogenesis, and neurosciences*, edited by E. Teramoto, M. Yamaguti (Springer, New York, 1987), p. 267
26. N.F. Rulkov, *Phys. Rev. Lett.* **86**, 183 (2001)
27. N.F. Rulkov, *Phys. Rev. E* **65**, 041922 (2002)
28. A. Shilnikov, N.F. Rulkov, *Phys. Lett. A* **328**, 177 (2004)
29. N.F. Rulkov, I. Timofeev, M. Bazhenov, *J. Comput. Neurosci.* **17**, 203 (2004)
30. D.V. Ramana Reddy, A. Sen, G.L. Johnston, *Phys. Rev. Lett.* **80**, 5109 (1998)
31. I. Ozden, S. Venkataramani, M.A. Long, B.W. Connors, A.V. Nurmikko, *Phys. Rev. Lett.* **93**, 158102 (2004)
32. J.J. Suarez-Vargas, J.A. Gonzales, A. Stefanovska, P.V.E. McClintock, *Europhys. Lett.* **85**, 38008 (2009)
33. B.S. Gutkin, J. Jost, H.C. Tuckwell, *Europhys. Lett.* **81**, 20005 (2008)
34. E. Rossoni, Y. Chen, M. Ding, J. Feng, *Phys. Rev. E* **71**, 061904 (2005)
35. M.A. Komarov, G.V. Osipov, J.A.K. Suykens, *Chaos* **18**, 037121 (2008)
36. N. Burić, K. Todorović, N. Vasović, *Phys. Rev. E* **78**, 036211 (2008)
37. K. Tsaneva-Atanasova, C.L. Zimlik, R. Bertram, A. Sherman, *Biophys. J.* **90**, 3434 (2006)
38. G. Tanaka, B. Ibarz, M.A.F. Sanjuán, K. Aihara, *Chaos* **16**, 013113 (2006)
39. C.A.S. Batista, A.M. Batista, J.A.C. de Pontes, R.L. Viana, S.R. Lopes, *Phys. Rev. E* **76**, 016218 (2007)
40. J.M. Casado, *Phys. Rev. Lett.* **91**, 208102 (2003)
41. P.F. Rowat, A.I. Selverston, *J. Comput. Neurosci.* **4**, 103 (1997)
42. D. Somers, N. Koppel, *Biol. Cybernet.* **68**, 393 (1993)
43. *Handbook of brain theory and neural networks*, edited by M.A. Arbib (MIT Press, Cambridge, 2003), p. 47
44. P. Varona, J.J. Torres, R. Huerta, H.D.I. Abarbanel, M.I. Rabinovich, *Neural Netw.* **14**, 865 (2001)
45. L.C. Yu, Y. Chen, P. Zhang, *Eur. Phys. J. B* **59**, 249 (2007)
46. W. Liu, J. Xiao, J. Yang, *Phys. Rev. E* **72**, 057201 (2005)
47. W. Zou, M. Zhan, *Phys. Rev. E* **80**, R065204 (2009)
48. K. Konishi, *Phys. Rev. E* **68**, 067202 (2003)
49. F.M. Atay, *Phys. Rev. Lett.* **91**, 094101 (2003)
50. A. Prasad, *Phys. Rev. E* **72**, 056204 (2005)
51. J. Garcia-Ojalvo, M.B. Elowitz, S.H. Strogatz, *PNAS* **101**, 10955 (2004)
52. E. Glatt, M. Gassel, F. Kaiser, *Europhys. Lett.* **81**, 40004 (2008)
53. R. Quian Quiroga, A. Kraskov, T. Kreuz, P. Grassberger, *Phys. Rev. E* **65**, 041903 (2002)
54. R. Quian Quiroga, T. Kreuz, P. Grassberger, *Phys. Rev. E* **66**, 041904 (2002)
55. T. Kreuz, F. Mormann, R. Andrzejak, A. Kraskov, K. Lehnertz, P. Grassberger, *Physica D* **225**, 29 (2007)
56. S.H. Strogatz, *Physica D* **143**, 1 (2000)
57. S.J. Wang, X.J. Xu, Z.X. Wu, Z.G. Huang, Y.H. Wang, *Phys. Rev. E* **78**, 061906 (2008)
58. D. Hennig, L. Schimansky-Geier, *Phys. Rev. E* **76**, 026208 (2007)
59. R.A. Stefanescu, V.K. Jirsa, *PLoS Comput. Biol.* **4**, e1000219 (2008)
60. J. Feng, V.K. Jirsa, M. Ding, *Chaos* **16**, 015109 (2006)
61. G.X. Qi, H.B. Huang, H.J. Wang, X. Zhang, L. Chen, *Europhys. Lett.* **74**, 733 (2006)
62. R. Erichsen, L.G. Brunnet, *Phys. Rev. E* **78**, 061917 (2008)
63. *Coordinated Activity in the Brain*, edited by J.L. Perez Velazquez, R. Wennberg (Springer, New York, 2009)
64. I. Franović, V. Miljković, *Phys. Rev. E* **79**, 061923 (2009)
65. P. Ostborn, *Phys. Rev. E* **79**, 051114 (2009)
66. J. Yang, *Phys. Rev. E* **76**, 016204 (2007)